Advanced Devices & Instrumentation
A SCIENCE PARTNER JOURNAL

RESEARCH ARTICLE

Ultracompact Multimode Meta-Microscope Based on Both Spatial and Guided-Wave Illumination

Xin Ye[1], Jiacheng Sun[1], Wei Jiang[2], Rongtao Yu[1], Chen Chen[1], Xingjian Xiao[1], Xiao Qian[1], Chunyu Huang[1], Yong Hu[2], Shining Zhu[1], and Tao Li[1]*

[1]National Laboratory of Solid State Microstructures, Key Laboratory of Intelligent Optical Sensing and Integration, Jiangsu Key Laboratory of Artificial Functional Materials, College of Engineering and Applied Sciences, Nanjing University, Nanjing 210093, China. [2]Institute of Materials Engineering, College of Engineering and Applied Sciences, Nanjing University, Nanjing 210093, China.

*Address correspondence to: taoli@nju.edu.cn

Citation: Ye X, Sun J, Jiang W, Yu R, Chen C, Xiao X, Qian X, Huang C, Hu Y, Zhu S, et al. Ultracompact Multimode Meta-Microscope Based on Both Spatial and Guided-Wave Illumination. *Adv. Devices Instrum.* 2023;4:Article 0023. https://doi.org/10.34133/adi.0023

Submitted 10 May 2023
Accepted 22 August 2023
Published 8 September 2023

Copyright © 2023 Xin Ye et al. Exclusive licensee Beijing Institute of Aerospace Control Devices. No claim to original U.S. Government Works. Distributed under a Creative Commons Attribution License 4.0 (CC BY 4.0).

Microscopic imaging technology is an indispensable foundation in the biomedical field, which enables powerful capability in bio-investigations. Aiming for more convenience and adaptability, a multifunctional microscope with a miniaturized scheme is a new requirement, but remains a challenge. Here, we propose an ultracompact microscope based on both spatial and guided-wave illumination that can work in bright-field, dark-field, and fluorescence imaging modes separately and simultaneously by conveniently switching the light source. The proposed guided-wave illumination not only provides a noise-free imaging mode, but also further reduces the system size. Moreover, a metalens array is specifically designed by a hexagonal arrangement to enable multi-field imaging and enlarge the field of view. The experiment results demonstrate that the half-pitch resolution is about 714 nm with an imaging magnification of 3.5×, with a field of view of 0.543 mm^2 and a space-bandwidth product of 4.26 megapixels. As examples, the multimode microscope is applied to image different cells and flowing microspheres in microtubules, showing comparable image quality with the images taken through the traditional microscope under guided-wave illumination. This demonstrates the possibility of the meta-microscope to be combined with microfluidic technology and further realize miniaturized microfluidic imaging systems. Our ultracompact multimode microscope has shown powerful capabilities for a new scheme of bio-observation and investigations.

Introduction

Versatility and miniaturization of imaging systems are of great importance in today's information society [1–7]. Microscopic imaging techniques have always been indispensable for scientific research and disease diagnosis in the biomedical field. The most commonly utilized imaging techniques are bright-field, dark-field, and fluorescence imaging, which are normally based on cumbersome optical components [8,9], such as eyepiece, objective lens, dichroic mirror, filter, and the sample holder. For fluorescence and dark-field microscopy, blocking unwanted light to ensure the darkest background is of substantial importance in imaging performance. In general, different methods are applied to remove the stray light for dark-field (oblique illumination) and fluorescence (with dichroic mirror and filter) microscopy, so that these imaging systems are always separated. The emergency of guided-wave illumination [10–15] makes it possible to combine 2 imaging techniques together, but the systems are still bulky and complicated.

A promising approach to accessing compact microscopes is to use metasurface/metalens [16–20], which consists of subwavelength nanostructures with powerful capabilities to modulate the amplitude and phase of light. As has been widely witnessed, metasurface optics provides an excellent platform to realize planar photonic devices with on-demand functionalities [21–29]. Some innovative metalenses have been demonstrated for fluorescence microscopy [30–34], but they have only been used as a substitute of a component in sophisticated imaging systems, and the advantages of an ultrathin and flat architecture have not been revealed or taken for use. Recently, highly compact microscopes [35,36] are proposed by directly integrating the metasurfaces on the complementary metal-oxide semiconductor (CMOS) image sensor, which significantly downsizes the imaging system. However, its imaging mode is fixed in bright-field due to the singlet illumination scheme.

In this work, we report a miniaturized multimode microscope for bright-field, dark-field, and fluorescence imaging by introducing the guided-wave illuminations. By conveniently switching the light source, 3 imaging modes can work together or separately within a very compact microscope (several centimeters in size). Notably, the proposed guided-wave illumination module not only provides a low noise imaging mode, but also further reduces the system size that favors the compact microscope very much. As a result, a metalens array is designed

and fabricated with a magnification of 3.5× in imaging (working at $\lambda = 470$ nm) after being integrated with the CMOS image sensor, which corresponds to the emission wavelength of fluorescence imaging. The imaging resolution is approximately 714 nm, ensuring subcellular imaging. The multimode microscope is then applied in various scenarios to validate its imaging capabilities in multiple modes, including fluorescent cells and microspheres in microtubules.

Materials and Methods

Numerical simulations

Numerical simulations are performed using the finite-difference time-domain methods. Rectangular silicon nitride (SiN*x*) nanofins with a fixed height of 1 μm are arranged on a fused-silica substrate with a lattice constant of 300 nm. The wavelength is 470 nm, and the refractive index is $n = 2.0$. The incident plane wave is polarized along *x* or *y* axes, and illuminates the nanofins from the substrate side. For sweeping the individual nanofins, perfectly matched layer conditions in the direction of the light propagation and periodic boundary conditions along all the in-plane directions were used. The phase shifts (φ_x and φ_y) and intensity of transmission coefficients (T_x and T_y) are obtained by parameter sweeping of the in-plane dimensions (L and W) of the nanofins by varying them between 80 and 240 nm at an interval of 5 nm (Fig. S1).

Sample fabrication

The SiN*x* layer was deposited on a 500-μm-thick fused silica substrate by plasma-enhanced chemical vapor deposition at 300 °C to a final thickness of 1 μm. Then, a positive electron beam resist (200 nm, PMMA A4) was spin-coated onto the substrate and baked at 170 °C for 5 min. Next, a 42-nm-thick layer of a water-soluble conductive polymer (AR-PC 5090) was spin-coated on the resist for the dissipation of electron beam charges. The metalens pattern was written on an electron beam resist using electron beam lithography (EBL, ELS-F125, Elionix). The conductive polymer was then dissolved in water and the resist was developed in a resist developer solution. Then, the pattern was transferred into a 40-nm-thick chromium layer deposited by electron beam evaporation (EBE) using the lift-off technique. The pattern chromium served as a hard mask for the dry etching of the 1-μm-thick SiN*x* layer in a mixture of CHF3 and SF6 plasma (Oxford Instruments, PlasmaPro100 Cobra300). Finally, the chromium mask was removed using a solution of ammonium cerium nitrate.

Optical measurement

For focusing characterization, a white-light laser (Fianium Super-continuum, 4 W) with a bandpass filter of 470 nm (Thorlabs, FB470-10) was used as the light source. Two orthogonal circularly polarized filters (thickness = 220 μm) were employed to generate the required polarization incidence and corresponding analyzer. An objective (numerical aperture [NA] = 0.42, 50×) and a CMOS image sensor (imaging source: DFK 27AUJ003, pixel size: 1.67 μm × 1.67 μm) are mounted on a translation motorized stage and move together along the propagation direction to capture light intensity profiles. For imaging characterization, a white light-emitting diode (LED) (Daheng Optics GCI-060411) with a bandpass filter of 470 nm (Thorlabs, FB470-10) and a diffuser film were employed as the illumination source. The image module is mounted on an assembled translation stage, which can be carefully adjusted along the optical direction to tune object distance during imaging (Fig. S2).

Results

Device design and architecture

Figure 1A shows the basic principle of the guided-wave illumination. The illumination light from the edge light source is coupled into the glass slide via the edge, and then the majority light propagates along the slide as a guided mode, which lights up the entire slide with evanescent waves bounded on the vicinity of the slide surface. When the specimens are placed on the surface, the evanescent wave of guided light will be scattered out and be captured by a certain lens, where the imaging is background illumination light free. As for the fluorescence imaging, the traditional scheme is illustrated in Fig. 1B, where the epi-fluorescent illumination is necessary with employment of a dichroic mirror and filters in the setup. Fortunately, our guided-wave illumination offers the opportunity to efficiently combine fluorescence imaging and dark-field imaging together (see Fig. 1A). For a compact integration, here we propose double-sided guided-wave illuminations as marked by mode II and mode III in Fig. 1C (see Fig. S3 for details of the setup and results of the guided-wave illumination used in traditional microscope), where the LED for mode II is blue ($\lambda = 470 \pm 5$nm, SMD5730) for dark-field imaging and the other is ultraviolet ($\lambda = 365$ nm, SMD 2835) for fluorescence imaging. The transmitted illumination (blue LED) is also compatible (marked as mode I) for the bright mode in the same compact microscope.

Figure 1D shows the photograph of the device composed of an illumination module, a glass slide, and an imaging module, where the glass slide not only works as a sample holder for the specimens, but also as a plate waveguide to guide the light emitted from the glass edge to illuminate the specimens. The imaging module is another important component of our multimode microscope. The inset of Fig. 1D shows that the metalens is sandwiched between 2 layers of the circular polarization filter (thickness of 220 μm), which can filter out the background light, and enable high signal-to-noise ratio (SNR) without emission filter for fluorescence imaging. The emission filter is unnecessary because of the effectiveness of guided-wave illumination and the purpose of system simplification. An additional substrate is used to increase the object distance, thereby building a magnification imaging system. Then, an ultracompact imaging module is implemented by directly pinning a polarization-filtered metalens to the CMOS image sensor (imaging source: DMM27UJ003-ML, pixel size: 1.67 μm × 1.67 μm) with the help of optically clear adhesive tapes (OCA, thickness: 50 μm, Tesa, 69402). Specifically, the imaging module is feasible for all modes simultaneously since the operating wavelengths for bright-field and dark-field imaging are the same as the fluorescence emission wavelength.

Design and optical characterizations of a singlet metalens

Figure 2A shows the photograph and scanning electron microscope (SEM) image of the fabricated metalens, which is designed using the Pancharatnam-Berry phase [37,38] that can work with a polarizer to further improve the contrast of the amplification imaging (see Fig. S5 for details of comparison

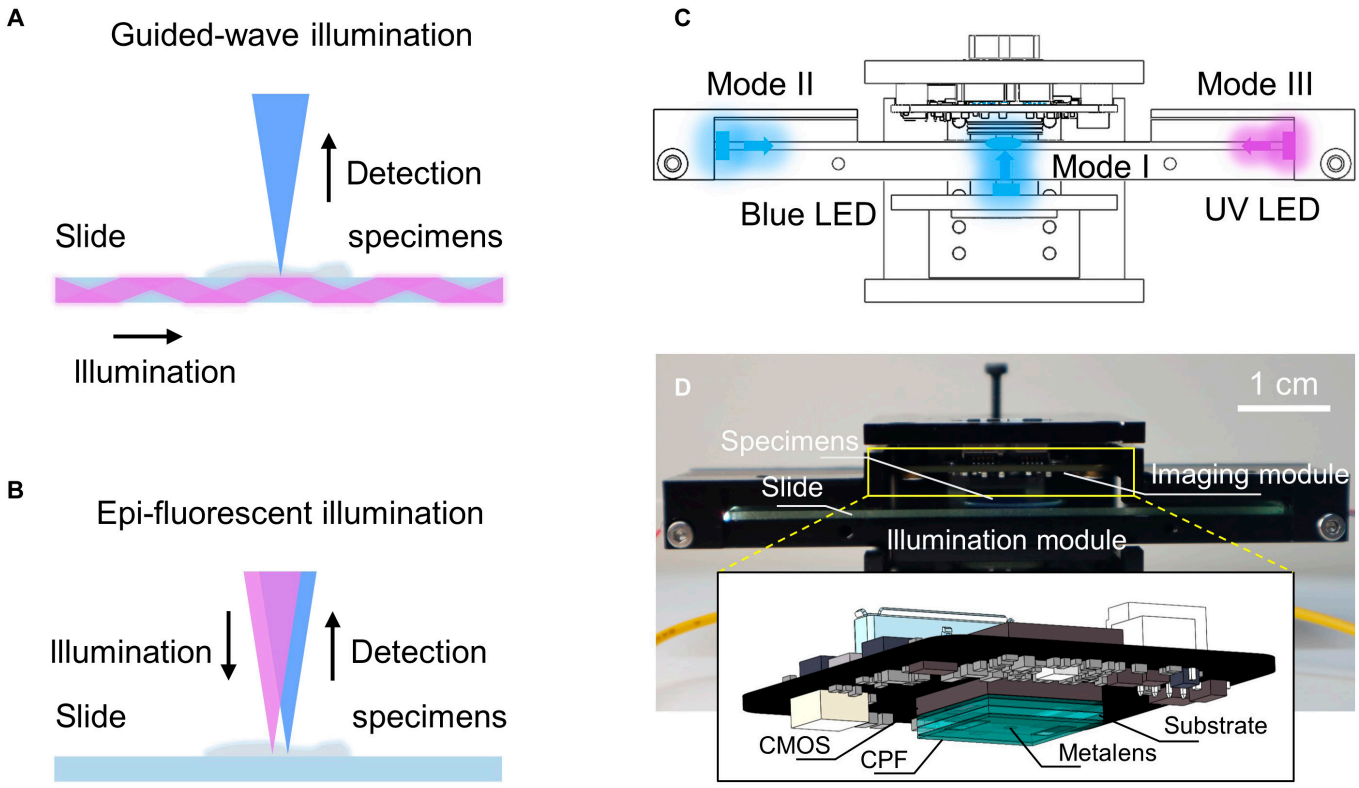

Fig. 1. Device design and architecture. (A) Schematic diagram of guided-wave illumination. The illumination direction is orthogonal to the detection direction. (B) Schematic diagram of epi-fluorescent illumination. The illumination direction is parallel to the detection direction. (C) Schematic illustration of the multimode microscope, composed of illumination and imaging modules. Mode I: bright-field imaging, mode II: dark-field imaging, and mode III: fluorescence imaging. (D) Photographic image of the multimode microscope (main body: $3 \times 3.7 \times 4.35$ cm^3, double-sided illumination module: $9.3 \times 3.2 \times 0.93$ cm^3, see Fig. S4) and inset for the schematic of the imaging module. The metalens is on the lower surface of the below substrate.

with metalens designed by propagation phase). The phase profile of the metalens based on the generalized laws of refraction satisfies [16]

$$\phi(R) = \frac{2\pi}{\lambda}\left(- \sqrt{s^2 + R^2} - \sqrt{\left(\frac{sf}{s-f}\right)^2 + R^2} \right) \quad (1)$$

where λ is the working wavelength, s is the object distance, R is the position of each nanofin in the radius dimension, and f is the focal length. The generalized aplanatic phase profile is applied to correct the aberration with respect to the high NA metalens [25]. The metalens contains SiNx nanofins arranged periodically in a square lattice with a constant $p = 300$ nm to satisfy the Nyquist-Shannon sampling theorem [39]. We choose SiNx as the material due to its relatively large refractive index, low loss in visible light, and potential compatibility with full CMOS-based devices. Each nanofin has equal height ($H = 1$ μm), length ($L = 240$ nm), and width ($W = 100$ nm) and acts as a half-wave plate with a high transmission efficiency. A 400-μm-diameter metalens was fabricated using standard electron-beam lithography and dry etching in a 1-μm-thick SiNx film deposited on the fused silica substrate (see Materials and Methods for details of sample fabrication) with focal length and object distance equal to 330 μm and 424 μm (NA = 0.52) at 470 nm corresponding to fluorescence emission wavelength and blue LED wavelength.

In experiments, we characterize the focusing and imaging of the designed polarization-filtered metalens with a homemade optical setup (see Materials and Methods for details of the measurement procedure and setup). First, the focusing performance is demonstrated as it is illuminated by a white-light laser (Fianium Super-continuum, 4W) with a 10-nm bandpass filter centered at 470 nm. Figure 2B shows the intensity profiles of the focal plane measured in the experiment and simulation, with the full width at half maximum (FWHM) equal to 771 nm and 719 nm, respectively. The simulation procedure is based on the Huygens-Fresnel principle [40] (see Note SI and Fig. S6). In order to obtain the intensity profiles of the axial plane (see Fig. 2C), optical intensity distribution was captured in several planes parallel to the focal plane. The experimentally measured focal length agrees well with the design. The modulation transfer functions (MTFs) of the metalens are computed based on the point spread functions from the experiment and simulation to provide a quantitative assessment of imaging capability. As displayed in Fig. 2D, the MTFs of the experiment are consistent with those of the simulation, while both are reasonably below the diffraction limit because the aplanatic phase design is particular for the spherical wave while the measurements here are referenced with the collimated incidence.

Next, a resolution chart (Edmund, #37-539 High Res Microscopy Target) was employed to test the imaging performance of the whole imaging module, as illustrated in Fig. 2E. Here, the white LED is used as the light source with a bandpass

filter centered at 470 nm and a 10-nm FWHM. Figure 2F displays the intensity distribution of the yellow vertical line in Fig. 2E, corresponding to the resolution of 700 lines per millimeter (about 714 nm).

Multimode imaging with a singlet metalens

After a basic characterization, the whole multimode microscope is employed for multimode imaging of diverse specimens. The photographs of the device working in 3 modes are shown in Fig. 3A to C, respectively, where it can be clearly distinguished that the illuminations come from 3 directions. The bright-field mode, which captures the transmitted light, is illuminated by the bottom LED light, while the dark-field and fluorescence modes are illuminated by the guiding light input from the slide edge. The proposed guided-wave illumination method effectively prohibits the undesired illumination light and ensures the high SNR.

The excitation and emission wavelength of the microscope are approximately 365 nm and 470 nm, respectively, where the emission wavelength at 470 nm is also the designed working wavelength for bright mode and dark mode. Thus, the microscope can work in multi-modes simultaneously. The blue fluorescence microspheres (FMSs, diameter D = 15 μm) were first observed as shown in Fig. 3D to F, where all the acquired images maintain comparable image quality to those taken by an Olympus microscope using the guided-wave illumination method (see Fig. S7 for more details of comparison results). Figure 3G to I shows the images of Hela cells, whose nucleus is stained with 4′,6-diamidino-2-phenylindole (DAPI). It is clear that the bright-field and dark-field imaging of Hela cells are relatively weaker than FMSs due to their small refractive index difference to the ambient solution (see Fig. S8 for more experimental imaging results). For unstained clear biological cells, the background noise increases as the intensity of the illumination increases in the dark-field

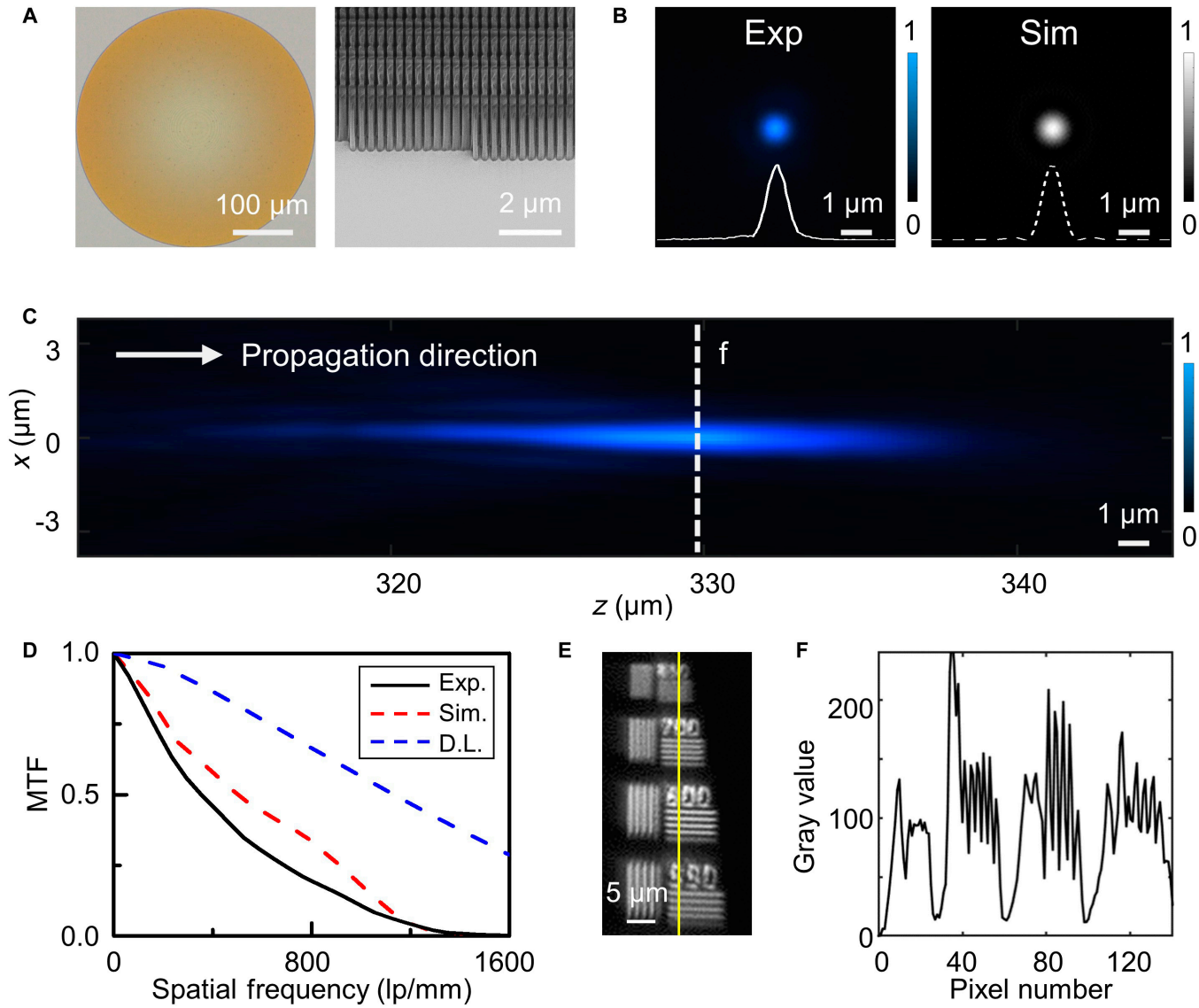

Fig. 2. Optical characterizations. (A) Top-view photographic image (left) and SEM image (right) of the fabricated metalens. (B) The intensity profiles of the focal plane by experiment (left) and simulation (right), respectively. (C) The intensity profiles of the axial plane with a center wavelength of 470 nm. The dashed line corresponds to the focal plane. (D) The experimental and simulated MTFs with respect to the diffraction-limited one. (E) The image of a resolution chart taken through the imaging module. (F) The intensity distribution of the yellow vertical line in (E), corresponding to the resolution of 700 lines per millimeter (about 714 nm).

mode, which captures the large-angle stray light. Obviously, the SNR of FMSs in the dark-field mode is better than that of Hela cells due to their large refractive index difference to the ambient solution. FMSs with a smaller size (D = 1 μm) were also observed, where a low-SNR fluorescence image and a good dark-field image were observed, showing a resolution of approximately 1.2 μm in the dark-field mode (Fig. S9).

Imaging results of DAPI-stained 4T1 cells with a metalens array

Since the field of view (FOV) is very important for an imaging system, various methods have been proposed to enlarge FOV in metalens imaging systems, such as quadratic phase [27,41–43] and metalens arrays [28,35,36]. In order to maximize the imaging FOV in our case, the area of the CMOS target plane of the multimode microscope should be fully utilized with more metalenses. It is noted that the flexibility of the metalens design makes it easy to arrange the metalenses. Here, the metalens array is arranged in a hexagonal pattern, as is shown in Fig. 4B, where the gray area corresponds to the area of the CMOS target plane, the blue-black circles correspond to the metalens array, and the red dotted circles correspond to the area (diameter = 3.75 × diameter of metalens) for each metalens to image without overlapping. Actually, NA for the single metalens is about 0.52, which introduces aberrations at the edge of the image results. Then, we added a suitable mask (a virtual field stop) to preserve the good-quality parts of the imaging results (see Figs. S10 and S11 for details of mask design and other discussions). Figure 4A shows the full CMOS effective FOV imaging results of 4T1 cells with 3 modes, where the SNR of dark-field imaging is relatively poor, while the other 2 modes achieve good imaging quality. We estimated that the diameter of the mask is about 240 μm, then the total FOV and space-bandwidth

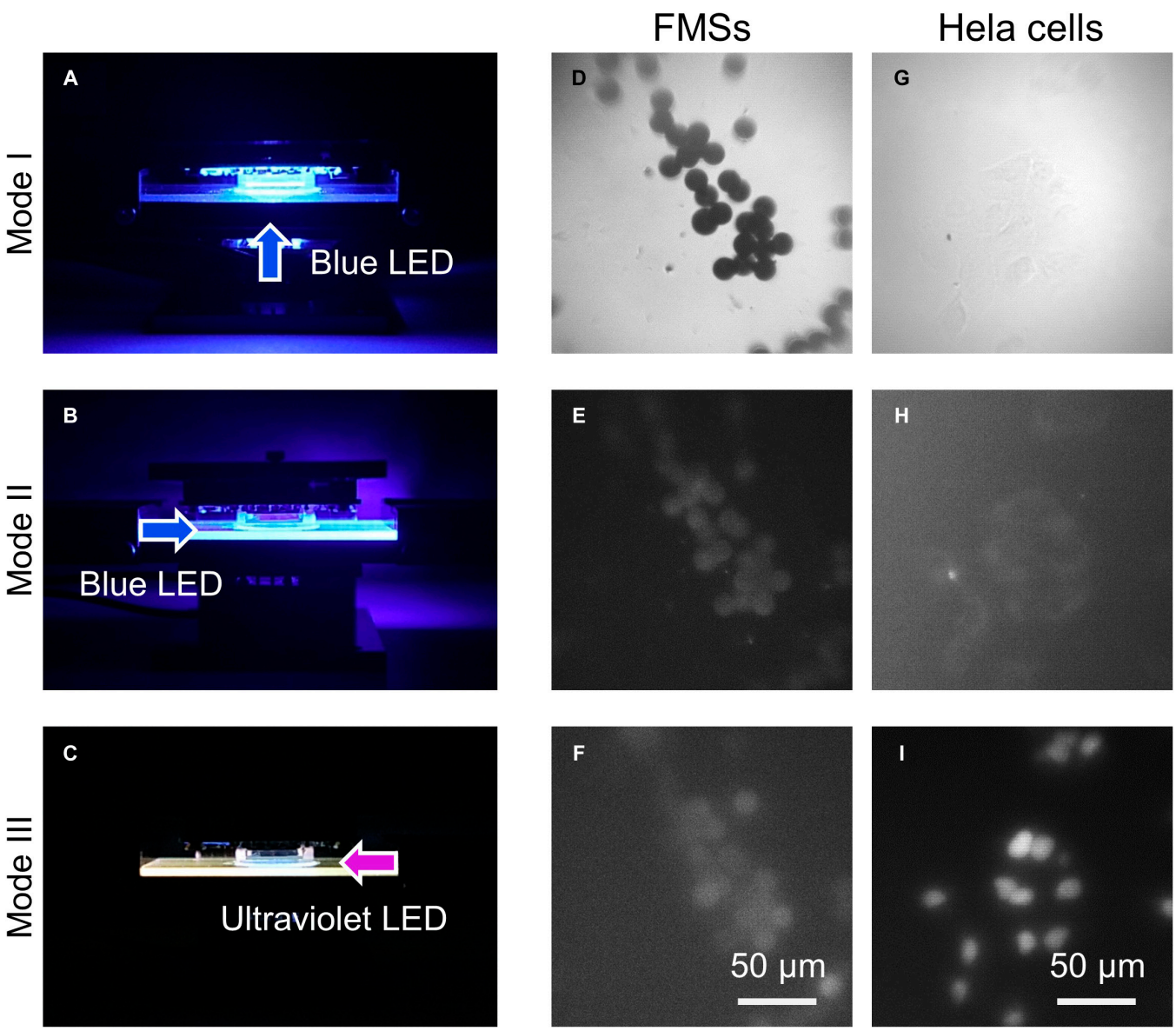

Fig. 3. Multimode imaging with a singlet metalens. Schematic diagrams of (A) mode I: bright-field imaging, (B) mode II: dark-field imaging, and (C) mode III: fluorescence imaging. (D to F) Images of the blue FMSs for 3 modes, respectively. (G to I) Images of DAPI-stained Hela cells for 3 modes, respectively.

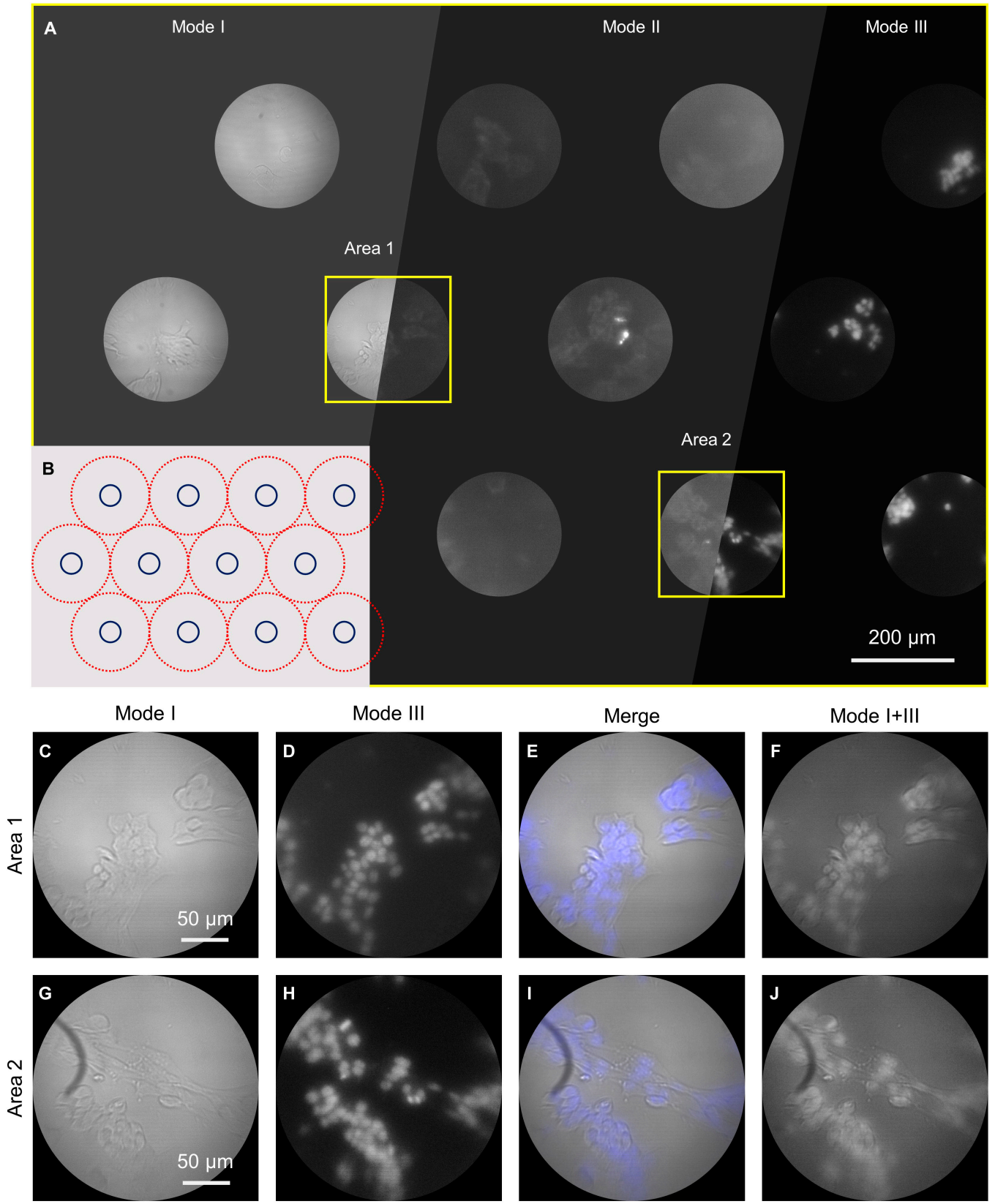

Fig. 4. Imaging results of DAPI-stained 4T1 cells. (A) The full-CMOS effective FOV imaging results of 4T1 cells by the multimode microscope. (B) Schematic illustration of the hexagonal arrangement of the metalens array: the gray area, dark blue circles, and red dotted circles correspond to the CMOS target plane, each metalens, and each imaging area, respectively. (C) The bright-field images of area 1 in (A). (D) The fluorescence images of area 1 in (A). (E) The manually merged image from (C) and (D). (F) The image of area 1 in (A) with simultaneous bright-field and fluorescence illumination. (G to J) The corresponding results of area 2 in (A).

product can be calculated as 0.543 mm^2 and 4.26 megapixels, respectively, which is better than other related works [2,10,44–48] (see Table S1).

Figure 4C and D and Fig. 4G and H show the imaging results of area 1 and area 2 in a single mode, respectively. The nuclei of 4T1 cells can be accurately located by manually merging images from bright-field and fluorescence imaging (see Fig. 4E and I). The merging procedure is done with the help of ImageJ, by adding the 2 imaging results to the corresponding color channel. Notably, in the multimode microscope, 2 imaging modes can be performed simultaneously (see Fig. 4F and J), which show comparable image quality with the merged images.

Multiple FOV imaging results of flowing FMSs in microfluidic channels

Moreover, further experiments were conducted to demonstrate the potential applications in microfluidic imaging techniques. Figure 5A shows the schematic diagram of the metalens array with microfluidic channels, where the microfluidics are composed of several borosilicate capillary micro glass slides (internal height: 0.1 mm, internal width: 0.1 mm, wall thickness: 0.09 mm, length: 50 mm). As shown in Fig. 5B, the bright-field image of the flowing blue FMSs in a single microfluidic channel is taken and the image results of more modes are shown in Fig. 5C to E

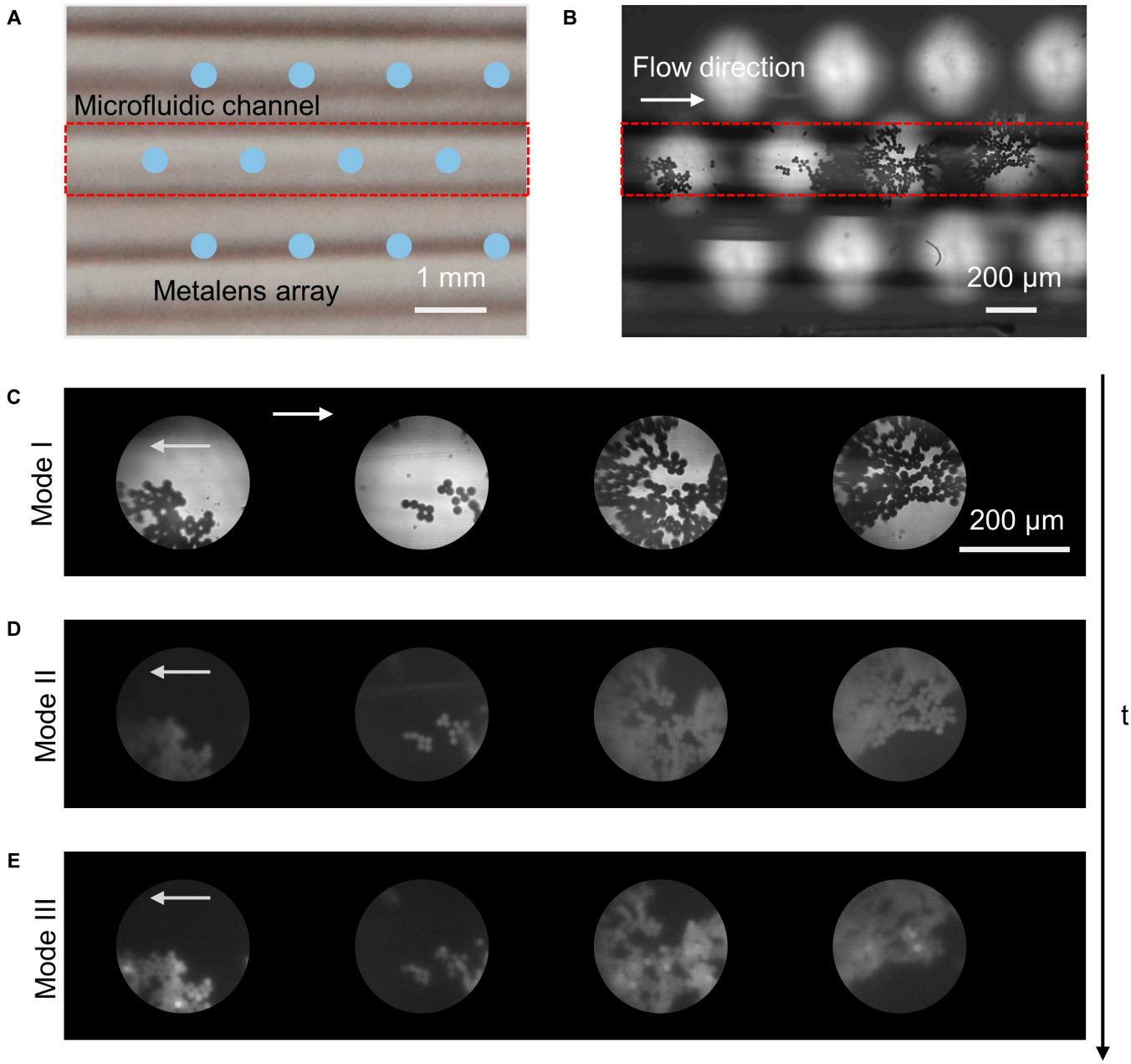

Fig. 5. Multiple FOV imaging results of flowing blue FMSs in microfluidic channels. (A) Image of microfluidic channels with the schematic metalens array. (B) Bright-field image of flowing blue FMSs in a single microfluidic channel. Zoomed-in images of (C) the bright-field, (D) the dark-field, and (E) the fluorescence one with the same area as the red box in (B). Due to the sequential time shooting, the images have a certain lateral offset.

(see Movie S1 for the flowing FMSs as an example). The image results have a certain lateral offset with respect to the time difference, and for the single-lens imaging system, the flow direction of the image is opposite to the actual flow direction. Based on the above, the multimode microscope has shown its potential to be combined with microfluidic technology instead of traditional bulky imaging systems and to further realize miniaturized microfluidic imaging systems.

Discussion

In conclusion, we proposed a miniaturized multimode microscope based on the guided-wave illumination and integrated metalens array. Three imaging modes including bright-field, dark-field, and fluorescence modes can be implemented in a centimeter-scale microscope. The proposed guided-wave illumination further saves the space to meet this compactness, which significantly combines the dark-field and fluorescence imaging together. The metalens array is specifically designed and works in a zoom-in mode with a magnification of 3.5× after being integrated with the CMOS image sensor, which is designed with respect to the wavelength of 470 nm corresponding to emission wavelength. The half-pitch resolution is about 714 nm, ensuring subcellular imaging resolution. As a result, for example, images for different specimens with 3 modes were taken, validating the imaging capability of this multimode microscope. This is the first meta-device implementation of multimode imaging in an ultracompact system, which is expected to enable real-time visualization of cell culture and to have a great impact in the biomedical field in the future.

Acknowledgments

Tao Li thanks the support from Dengfeng Project B of Nanjing University. The authors acknowledge the micro-fabrication center of the National Laboratory of Solid State Microstructures (NLSSM) for technique support. **Funding:** This work was supported by the National Key R&D Program of China (2022YFA1404301) and the National Natural Science Foundation of China (Nos. 12174186, 92250304, 62325504, and 62288101). **Author contributions:** X.Y. and T.L. conceived the idea. X.Y. proposed the design and performed the numerical simulations with the help of X.X. and C.C.; J.S. and C.H. fabricated the samples; W.J. and Y.H. provided the fluorescent biological samples; X.Y. and J.S. performed the optical measurements; R.Y. implemented the prototype with the help of X.Y. and X.Q.; X.Y. and T.L. analyzed the results and wrote the manuscript with the input from all authors; T.L. supervised the project. **Competing interests:** The authors declare that they have no competing interests.

Data Availability

All data needed to evaluate the conclusion in the paper are present in the paper or the supplementary materials.

Supplementary Materials

Supplementary Text
Figures S1 to S11
Table S1
Movie S1

References

1. Rane AS, Rutkauskaite J, deMello A, Stavrakis S. High-throughput multi-parametric imaging flow cytometry. *Chem*. 2017;3(4):588–602.
2. Dai B, Jiao Z, Zheng L, Bachman H, Fu Y, Wan X, Zhang Y, Huang Y, Han X, Zhao C, et al. Colour compound lenses for a portable fluorescence microscope. *Light Sci Appl*. 2019;8:75.
3. Xue Y, Davison IG, Boas DA, Tian L. Single-shot 3D wide-field fluorescence imaging with a computational miniature mesoscope. *Sci Adv*. 2020;6(43):eabb7508.
4. Yanny K, Antipa N, Liberti W, Dehaeck S, Monakhova K, Liu FL, Shen K, Ng R, Waller L. Miniscope3D: Optimized single-shot miniature 3D fluorescence microscopy. *Light Sci Appl*. 2020;9:171.
5. Lee KC, Lee K, Jung J, Lee SH, Kim D, Lee SA. A smartphone-based Fourier ptychographic microscope using the display screen for illumination. *ACS Photonics*. 2021;8(5):1307–1315.
6. Kim K, Jang K-W, Ryu J-K, Jeong K-H. Biologically inspired ultrathin arrayed camera for high-contrast and high-resolution imaging. *Light Sci Appl*. 2020;9:28.
7. Choi W, Kang M, Hong JH, Katz O, Lee B, Kim GH, Choi Y, Choi W. Flexible-type ultrathin holographic endoscope for microscopic imaging of unstained biological tissues. *Nat Commun*. 2022;13:4469.
8. Smith WJ. *Modern lens design*.New York: McGraw-Hill; 2004.
9. Gross H, Blechinger F, Achtner B. *Handbook of optical systems*.Weinheim: Wiley-VCH; 2005.
10. Sung Y, Campa F, Shih W-C. Open-source do-it-yourself multi-color fluorescence smartphone microscopy. *Biomed Opt Express*. 2017;8(11):5075–5086.
11. Diekmann R, Helle ØI, Øie CI, McCourt P, Huser TR, Schüttpelz M, Ahluwalia BS. Chip-based wide field-of-view nanoscopy. *Nat Photonics*. 2017;11:322–328.
12. Tinguely J-C, Helle ØI, Ahluwalia BS. Silicon nitride waveguide platform for fluorescence microscopy of living cells. *Opt Express*. 2017;25(22):27678–27690.
13. Yang T, Liu Y-H, Mu Q, Zhu M, Pu D, Chen L, Huang W. Compact compound-eye imaging module based on the phase diffractive microlens array for biometric fingerprint capturing. *Opt Express*. 2019;27(5):7513–7522.
14. Archetti A, Glushkov E, Sieben C, Stroganov A, Radenovic A, Manley S. Waveguide-PAINT offers an open platform for large field-of-view super-resolution imaging. *Nat Commun*. 2019;10:1267.
15. Jang K-W, Kim K, Bae S-I, Jeong K-H. Biologically inspired ultrathin contact imager for high-resolution imaging of epidermal ridges on human finger. *Adv Mater Technol*. 2021;6(8):Article 2100090.
16. Yu N, Genevet P, Kats MA, Aieta F, Tetienne J-P, Capasso F, Gaburro Z. Light propagation with phase discontinuities: Generalized laws of reflection and refraction. *Science*. 2011;334(6054):333–337.
17. Sun S, He Q, Xiao S, Xu Q, Li X, Zhou L. Gradient-index meta-surfaces as a bridge linking propagating waves and surface waves. *Nat Mater*. 2012;11:426–431.
18. Kildishev AV, Boltasseva A, Shalaev VM. Planar photonics with metasurfaces. *Science*. 2013;339(6125):1232009.
19. Kamali SM, Arbabi E, Arbabi A, Faraon A. A review of dielectric optical metasurfaces for wavefront control. *Nanophotonics*. 2018;7(6):1041–1068.

20. Li T, Chen C, Xiao X, Chen J, Hu S, Zhu S. Revolutionary meta-imaging: From superlens to metalens. *Photonics Insights*. 2023;2(1):R01.
21. Khorasaninejad M, Chen WT, Devlin RC, Oh J, Zhu AY, Capasso F. Metalenses at visible wavelengths: Diffraction-limited focusing and subwavelength resolution imaging. *Science*. 2016;352(6290):1190–1194.
22. Khorasaninejad M, Capasso F. Metalenses: Versatile multifunctional photonic components. *Science*. 2017;358(6367):Article eaam8100.
23. Lee G-Y, Hong J-Y, Hwang S, Moon S, Kang H, Jeon S, Kim H, Jeong J-H, Lee B. Metasurface eyepiece for augmented reality. *Nat Commun*. 2018;9:4562.
24. Faraji-Dana M, Arbabi E, Arbabi A, Kamali SM, Kwon H, Faraon A. Compact folded metasurface spectrometer. *Nat Commun*. 2018;9:4196.
25. Chen C, Song W, Chen J-W, Wang J-H, Chen YH, Xu B, Chen M-K, Li H, Fang B, Chen J, et al. Spectral tomographic imaging with aplanatic metalens. *Light Sci Appl*. 2019;8:99.
26. Zhou Y, Zheng H, Kravchenko II, Valentine J. Flat optics for image differentiation. *Nat Photonics*. 2020;14:316–323.
27. Luo X, Zhang F, Pu M, Guo Y, Li X, Ma X. Recent advances of wide-angle metalenses: Principle, design, and applications. *Nanophotonics*. 2022;11(1):1–20.
28. Chen J, Ye X, Gao S, Chen Y, Zhao Y, Huang C, Qiu K, Zhu S, Li T. Planar wide-angle-imaging camera enabled by metalens array. *Optica*. 2022;9(4):431–437.
29. Pan M, Fu Y, Zheng M, Chen H, Zang Y, Duan H, Li Q, Qiu M, Hu Y. Dielectric metalens for miniaturized imaging systems: Progress and challenges. *Light Sci Appl*. 2022;11:195.
30. Arbabi E, Li J, Hutchins RJ, Kamali SM, Arbabi A, Horie Y, Dorpe PV, Gradinaru V, Wagenaar DA, Faraon A. Two-photon microscopy with a double-wavelength metasurface objective lens. *Nano Lett*. 2018;18(8):4943–4948.
31. Jang M, Horie Y, Shibukawa A, Brake J, Liu Y, Kamali SM, Arbabi A, Ruan H, Faraon A, Yang C. Wavefront shaping with disorder-engineered metasurfaces. *Nat Photonics*. 2018; 12:84–90.
32. Wang Y, Chen Q, Yang W, Ji Z, Jin L, Ma X, Song Q, Boltasseva A, Han J, Shalaev VM, et al. High-efficiency broadband achromatic metalens for near-IR biological imaging window. *Nat Commun*. 2021;12(1):5560.
33. Luo Y, Chu CH, Vyas S, Kuo HY, Chia YH, Chen MK, Shi X, Tanaka T, Misawa H, Huang Y-Y, et al. Varifocal metalens for optical sectioning fluorescence microscopy. *Nano Lett*. 2021;21(12):5133–5142.
34. Luo Y, Tseng ML, Vyas S, Hsieh T-Y, Wu J-C, Chen S-Y, Peng H-F, Su V-C, Huang T-T, Kuo HY, et al. Meta-lens light-sheet fluorescence microscopy for *in vivo* imaging. *Nanophotonics*. 2022;11(9):1949–1959.
35. Xu B, Li H, Gao S, Hua X, Yang C, Chen C, Yan F, Zhu S, Li T. Metalens-integrated compact imaging devices for wide-field microscopy. *Adv Photonics*. 2020;2:Article 066004.
36. Ye X, Qian X, Chen Y, Yuan R, Xiao X, Chen C, Hu W, Huang C, Zhu S, Li T. Chip-scale metalens microscope for wide-field and depth-of-field imaging. *Adv Photonics*. 2022;4:Article 046006.
37. Bomzon Z, Biener G, Kleiner V, Hasman E. Space-variant Pancharatnam–Berry phase optical elements with computer-generated subwavelength gratings. *Opt Lett*. 2002;27:1141–1143.
38. Huang L, Chen X, Mühlenbernd H, Li G, Bai B, Tan Q, Jin G, Zentgraf T, Zhang S. Dispersionless phase discontinuities for controlling light propagation. *Nano Lett*. 2012;12(11):5750–5755.
39. Goodman JW. *Introduction to Fourier optics*. Greenwood Village: Roberts and Company Publishers; 2005.
40. Voelz DG. *Computational Fourier optics: A MATLAB tutorial*.Bellingham (WA): SPIE Press; 2011.
41. Pu M, Li X, Guo Y, Ma X, Luo X. Nanoapertures with ordered rotations: Symmetry transformation and wide-angle flat lensing. *Opt Express*. 2017;25(25):31471–31477.
42. Martins A, Li K, Li J, Liang H, Conteduca D, Borges B-HV, Krauss TF, Martins ER. On metalenses with arbitrarily wide field of view. *ACS Photonics*. 2020;7(8):2073–2079.
43. Zhang F, Pu M, Li X, Ma X, Guo Y, Gao P, Yu H, Gu M, Luo X. Extreme-angle silicon infrared optics enabled by streamlined surface. *Adv Mater*. 2021;33(11):Article 2008157.
44. Miller AR, Davis GL, Oden ZM, Razavi MR, Fateh A, Ghazanfari M, Abdolrahimi F, Poorazar S, Sakhaie F, Olsen RJ, et al. Portable, battery-operated, low-cost, bright field and fluorescence microscope. *PLOS ONE*. 2010;5(8):Article e11890.
45. Zhu H, Yaglidere O, Su T-W, Tseng D, Ozcan A. Cost-effective and compact wide-field fluorescent imaging on a cell-phone. *Lab Chip*. 2011;11:315–322.
46. Ghosh K, Burns L, Cocker E, Nimmerjahn A, Ziv Y, Gamal AE, Schnitzer M. Miniaturized integration of a fluorescence microscope. *Nat Methods*. 2011;8:871–878.
47. Zhu H, Mavandadi S, Coskun AF, Yaglidere O, Ozcan A. Optofluidic fluorescent imaging cytometry on a cell phone. *Anal Chem*. 2011;83:6641–6647.
48. Wei Q, Qi H, Luo W, Tseng D, Ki SJ, Wan Z, Göröcs Z, Bentolila LA, Wu T-T, Sun R, et al. Fluorescent imaging of single nanoparticles and viruses on a smart phone. *ACS Nano*. 2013;7(10):9147–9155.